

3D printing of shape memory poly(D,L-lactide-co-trimethylene carbonate) by direct ink writing for shape-changing structures

Xue Wan,¹ Hongqiu Wei,¹ Fenghua Zhang,¹ Yanju Liu,² Jinsong Leng¹ 

¹National Key Laboratory of Science and Technology on Advanced Composites in Special Environments, Harbin Institute of Technology, Harbin 150080, People's Republic of China

²Department of Astronautical Science and Mechanics, Harbin Institute of Technology, Harbin 150001, People's Republic of China

Correspondence to: J. Leng (E-mail: lengjs@hit.edu.cn)

ABSTRACT: Four-dimensional (4D) printing of shape memory materials has attracted increasing interests for personalized structures. In this study, a biocompatible poly(D,L-lactide-co-trimethylene carbonate) (PLMC) is utilized to fabricate 4D shape-changing structures with customized geometries through direct ink writing. The printed objects show shape transformations at different dimensions under thermal programming. The influence of the printing parameters on the properties including rheological, solvent evaporation, and static mechanical behavior are systematically investigated. A printing map is further depicted to achieve high-quality printing with high viscous ink flowed from micronozzle to construct various structures. The printed structures in one-dimensional, two-dimensional, and three-dimensional (3D) exhibit shape-changing behavior with fast response around body temperature. The fast responsive time shows potential in the field of surgical suture (4 s), nonwoven fabric (3 s), and self-expandable stent (35 s). The feasibility of 3D printing of PLMC opens the way for applications in shape-changing devices with small diameter. © 2019 Wiley Periodicals, Inc. *J. Appl. Polym. Sci.* **2019**, *136*, 48177.

KEYWORDS: direct ink writing; poly(D,L-lactide-co-trimethylene carbonate); printing parameters; shape-changing devices; shape memory polymer

Received 23 February 2019; accepted 29 May 2019

DOI: 10.1002/app.48177

INTRODUCTION

Shape memory polymers (SMPs), an important branch of stimuli-responsive smart materials, are characterized by shape morphing behavior from a temporary shape recovering to their original shape triggered by an external stimulus.^{1–5} Owing to their intrinsic shape-changing capability, SMPs have been explored for applications in space deployable structures,^{6,7} flexible electronics,^{8,9} soft robotics,¹⁰ artificial muscles,¹¹ smart actuators,¹² and textiles.¹³ Especially, these smart materials have attracted increasing academic interest in biomedical fields, such as self-tightening devices,^{14,15} biodegradable stents,^{16,17} drug delivery systems,^{16,18} porous scaffolds,¹⁹ thrombus removal device,²⁰ and microactuators.²¹ SMPs-based medical devices could be deformed to a small packed status in advance to go through narrow passages and recover to their original shapes later under appropriate stimulus. This feature is significantly promising in minimally invasive surgery.

Poly(D,L-lactic acid) is a polymer synthesized from D,L-lactic acid (DLA) monomers through melt polycondensation. It can degrade to lactic acid which can be easily metabolized by human body. In the past decades, this biocompatible SMP has been widely investigated in

biomedical applications.^{22–24} However, its drawback is obvious in high rigidity at body temperature,²⁵ long period of degradation,²⁶ and side effect of degradation product,²⁷ which limits its application as soft medical devices. An effective method is to copolymerize with other monomers, such as trimethylene carbonate (TMC), as a softening component to reduce glass transition temperature. Several studies have reported the fabrication of poly(DLLA-co-TMC) (abbreviated as PLMC) and the optimization of their thermal, physical, mechanical, and biodegradable properties by modulating the ratios of the monomers.^{28–31} In previous research, this copolymer with approximately 80 mol % of DLLA behaved well as biomaterial with high attachment and proliferation with human cells, displaying adequate material–cell interactions.^{31–33} However, the application of this biodegradable copolymer is far from fully exploited, as its intrinsic shape-changing characteristics are rarely focused.^{28,30,34} Meanwhile, traditional processing techniques are inadequate for constructing architectures with complex user-defined or microscale geometries. The structures fabricated by PLMC are mostly membranes or tubes through electrospinning or pouring material into a mold.^{28,29} Till now, it remains a challenge to achieve the building of personalized PLMC-based shape-changing structures for biomedical areas.

Additional Supporting Information may be found in the online version of this article.

© 2019 Wiley Periodicals, Inc.

Four-dimensional (4D) printing is an advanced manufacturing technique that enables three-dimensional (3D) printed structures' physical properties (e.g., shape, structure, dimension) to achieve self-transformation with the change of time under appropriate external stimulus.^{35–39} 4D printed poly(lactic acid) (PLA)-based SMP shows potential in biomedical application such as scaffold and braided tubes.^{35,40} However, the actuation temperature is around 80 °C, which is far higher than body temperature, making it difficult to be applied in biomedical field. To solve this problem, printing a new SMP with a lower actuation temperature is quite promising, such as PLMC. Fine structures can be constructed by direct ink writing (DIW) through layer-by-layer ink deposition.^{41–44} It is a flexible and laboratory-friendly printing technique based on its open source and a small amount of material compared to other techniques.

Herein, we demonstrate a simple and feasible strategy to fabricate 4D PLMC-based active shape-changing structures through DIW technique. We first modulated the rheological capability and solvent evaporation rate of PLMC ink to find the optimum printing parameters. A printing map was depicted to guide the construction of various architectures ranging from micro to macro, one-dimensional (1D) to 3D. The thermal, mechanical, and shape memory properties of the printed structures were characterized. The 4D printed PLMC-based structures showed shape-changing behavior at around 45 °C. We further explored the potential of these 4D structures to be applied in shape-changing applications such as minimally invasive fields.

EXPERIMENTAL

Materials

PLMC copolymers with a DLLA:TMC molar ratio of 80:20, abbreviated as PLMC, was purchased from Jinan Daigang Biomaterial Co., Ltd. (China). The weight-average molecular weight (M_w) and polydispersity index of the material, tested by gel permeation chromatography, were 420 kDa and 1.9, respectively. Dichloromethane (DCM) of analytical grade was received from Aladdin Industrial Inc. PLMC particles were dried in a vacuum oven at 40 °C for 12 h.

Preparation of PLMC Ink

PLMC inks were prepared by dissolving pure PLMC particles in DCM with varied weight ratios of 1/5, 1/6, and 1/7, denoted as PLMC 1/5, PLMC 1/6, and PLMC 1/7, respectively. The solutions were subsequently ultrasonicated at 40 kHz in sealed bottles for 1 h intermittently. Finally, they were placed at room temperature for adequate dissolution.

3D printing of PLMC solutions was accomplished by a robot system (I&J2200-4; I&J Fisanar), manipulated by a modeling software (JR Points for Dispensing; Janome Sewing Machine) and a pneumatic dispensing device (HP-7X, EFD). PLMC solutions were injected into a syringe (3 mL volume, EFD) located in the robot. The extrusion of PLMC ink through micronozzle was controlled by the computer program.

Rheological Characterization

Rheological property was characterized by the process-related viscosity of the polymer ink. PLMC 1/5, 1/6, and 1/7 were evaluated

by a capillary flow analysis based on a previous reported study.⁴⁵ A micronozzle of 200 μm was utilized for various inks. PLMC 1/6 was also extruded from nozzles with inner diameters of 160, 200, and 260 μm . The applied pressure was set ranging from 0.24 to 3.85 MPa. The inks were deposited into filaments at a velocity of 0.3 mm s^{-1} . The printed filaments were further dried in a 50 °C vacuum oven for 12 h. The dried filaments were weighed to obtain the mass flow rate, which was used to calculate the volumetric flow rate by dividing their respective ink densities. Considering the ink belonged to non-Newtonian fluid, the Rabinowitch–Mooney correction was established to revise the raw calculated capillary data. The end effects could be neglected because the ratio of the nozzle length to its diameter was over 50.⁴⁵

Solvent Evaporation Rate Characterization

Based on previous studies,⁴³ the solvent evaporation ability of DCM was investigated by printing a 5 mm filament on a glass slide resting on an electronic balance (ML104; Mettler-Toledo). The samples were printed using different inks (PLMC 1/5, 1/6, and 1/7) from a nozzle of 510 μm at the velocity rate of 1 mm s^{-1} under various pressures (2.8, 1.75, and 1.4 MPa, respectively). The utilization of different applied pressure was aimed to ensure the same diameter of the filaments or the same evaporation area. PLMC 1/6 was also printed using other two nozzles of 200 and 330 μm under the applied pressure of 3.5 and 2.45 MPa. The real-time mass of all the extruded filaments was recorded for 10 h. The filaments were then placed in a vacuum oven at 50 °C for completely drying. Then, the dried mass was considered as the pure solute mass. Thus, the solvent evaporation ability could be characterized by the real-time solvent percentage.

Fabrication of Structures and Morphology Characterization

1D and two-dimensional (2D) microstructures were fabricated using PLMC 1/6 extruded from a nozzle of 200 μm . The 1D filament was deposited at a velocity of 0.5 mm s^{-1} under an applied pressure of 1.4 MPa. Intricate 2D patterns of the horse and the sunflower were fabricated using an applied pressure of 1.75 MPa and 1 mm s^{-1} robot velocity. A combination of different parameters was implemented for 3D structures ranging from microscale to macroscale. The circular tower was extruded from PLMC 1/7 using a nozzle of 100 μm under 2.1 MPa and 0.4 mm s^{-1} . A circular spiral was built using PLMC 1/5 with a 160 μm nozzle under 2.45 MPa and 0.4 mm s^{-1} . The Gecko was built with PLMC 1/6 through a 200 μm nozzle under 3.5 MPa and 4 mm s^{-1} . The self-supporting structures (Latin capital letter “H, I, T”) were printed from PLMC 1/6 using a nozzle of 200 μm , under a 2.1 MPa applied pressure and a robot velocity of 2 mm s^{-1} . The scaffolds of a five-layer orthogonal pattern configuration (ORTH) and a four-layer displaced pattern configuration (DISP) were both fabricated from PLMC 1/6 using a micronozzle of 100 μm under a 2.45 MPa applied pressure and 0.5 mm s^{-1} robot velocity.

The morphologies of the structures were observed on a TESCAN VEGA3 scanning electron microscope (SEM). All the test specimens were prepared by sputtering gold for 20 s in advance. A set of images for shape-changing process was observed on an optical microscope (Olympus SZX16).

Dynamic Thermomechanical Measurements

Dynamic mechanical analysis (DMA) was determined using TA Q800 Instrument under film tension mode. The sample was tested at a frequency of 1 Hz, a preload of 0.001 N, an amplitude of 25 μm , and a heating rate of 5 $^{\circ}\text{C min}^{-1}$. The rectangular-shaped sample was printed ($30 \times 4 \times 0.8 \text{ mm}^3$) from PLMC 1/6 using a nozzle of 200 μm under the conditions of 2.1 MPa applied pressure and 2 mm s^{-1} robot velocity. The testing orientation for as-printed PLMC was along the printed direction of the filaments. Original PLMC pellets were dissolved in DCM to obtain a solvent-cast film with the same size to evaluate the intrinsic property of the material before printing.

Thermal Properties and Fourier Transform Infrared Spectroscopy Analysis

The thermal properties of preprinted and postprinted PLMC were measured using Mettler Toledo differential scanning calorimetry (DSC) system. The sample with a weight of 6–8 mg was scanned in a 25–200–25 $^{\circ}\text{C}$ cycle in nitrogen atmosphere, at a rate of 10 $^{\circ}\text{C min}^{-1}$.

The spectra of the preprinted and postprinted PLMC were analyzed by Fourier Transform Infrared Spectroscopy (FTIR; Spectrum Two; PerkinElmer Inc.) in a wavenumber range of 800–4000 cm^{-1} at a scanning resolution of 4 cm^{-1} .

Shape Memory Property Measurements

The shape memory effect was quantitatively assessed by the shape memory cycle (SMC) performed on DMA Q800 in a force controlled mode according to previous studies.^{46,47} The sample ($30 \times 4 \times 0.8 \text{ mm}^3$) was prepared the same as the DMA test. A preload of 0.01 N was set to fix the sample to prevent slip. The SMC test was performed in four steps.

1. Deformation: The printed sample was thermally equilibrated at T_d (deformation temperature slightly above T_g) for 5 min to obtain the initial strain ($\epsilon_{\text{initial}}$) and subsequently stretched isothermally from 0.01 to 0.25 N under a force rate of 0.05 N min^{-1} . The obtained strain was recorded as deformed strain (ϵ_{deform}).
2. Cooling: The specimen was cooled to 0 $^{\circ}\text{C}$ at a rate of 5 $^{\circ}\text{C min}^{-1}$, and then equilibrated for 5 min under constant external force.
3. Fixing: The external force was unloaded isothermally at a rate of 0.05 N min^{-1} and the specimen was equilibrated at 0 $^{\circ}\text{C}$ for 5 min to obtain the fixed strain (ϵ_{fix}).
4. Recovery: Reheated the specimen at a rate of 5 $^{\circ}\text{C min}^{-1}$ to T_d , then equilibrated for 10 min, the obtained strain was recorded as the residual strain after recovery ($\epsilon_{\text{recover}}$). Thus, the shape fixity ratio (R_f) as well as shape recovery ratio (R_r) were calculated as follows⁴⁴:

$$R_f (\%) = \frac{\epsilon_{\text{fix}}}{\epsilon_{\text{deform}}} \times 100\% \quad (1)$$

$$R_r (\%) = \frac{\epsilon_{\text{deform}} - \epsilon_{\text{recover}}}{\epsilon_{\text{deform}} - \epsilon_{\text{initial}}} \times 100\% \quad (2)$$

The SMC test was also performed on solvent-cast film using the same method.

The 3D printed structures (“H,” “I,” “T”) were heated to 60 $^{\circ}\text{C}$ which was slightly higher than T_g . Then, they were deformed to temporary shapes under an external force. When cooling down to room temperature, the temporary shape could be fixed. The thermoresponsive macroscopic shape-changing behavior was observed by immersing the structures into a water bath at 60 $^{\circ}\text{C}$. The shape recovery ratios were calculated by their dimensional changes.

Static Mechanical Properties

The filaments with 60 mm length were printed using various inks through different nozzles. They were stretched at a speed of 2 mm min^{-1} at room temperature using an Instron 5944 Universal Machine equipped with a 2 kN load cell. 1D filaments were also tested on DMA Q800 in the force controlled mode at 70 $^{\circ}\text{C}$, at a force rate of 0.5 N min^{-1} . At least five samples were tested.

Porosity of Scaffold

The theoretical volume porosity ratios of ORTH and DISP scaffolds were evaluated based on predesigned unit architectures with the hypothesis that the strut diameter and the spacing between two adjacent struts were equal. For theoretical analysis, we selected a unit of square cell for both patterns. Thus, the volume porosity could be calculated as follows:

$$V_{\text{porosity}} = \frac{V_{\text{unit}} - V_{\text{actual}}}{V_{\text{unit}}} \times 100\% \quad (3)$$

Herein, V_{unit} is the chosen unit volume = LWH , V_{actual} is the actual volume of the scaffold = $V_{\text{strut}}N_{xy}N_z$, V_{strut} represents the strut volume = $\pi D^2L/4$, and N_{xy} and N_z correspond to the number of struts per x - y layer and the number of layers along z axis per unit, respectively. Therefore

$$V_{\text{porosity}} = \left(1 - \frac{\pi D^2 N_{xy} N_z}{4WH} \right) \times 100\% \quad (4)$$

where D , L , W , and H refer to the strut diameter, strut length = $DN_{xy} + S(N_{xy}-1)$, unit width = strut length and unit height = DN_z , respectively, and S is the spacing distance between adjacent struts.

RESULTS AND DISCUSSION

Figure 1 illustrates the process of 4D printing shape memory PLMC through DIW. Figure 1(a) presents the molecular structure of PLMC. This thermoplastic polymer possesses excellent shape memory performance under heat stimulus. As demonstrated in SMC test shown in Figure 1(b), R_f and R_r of PLMC calculated by eqs. (1) and (2) reached 99.52 and 99.98%, respectively. The ink was prepared by dissolving PLMC in DCM with fast evaporation rate. The printing principle is schematically shown in Figure 1(c). PLMC ink was extruded through a customer-defined micronozzle under an appropriate applied pressure to construct structure layer by layer. The 4D shape-changing behavior was achieved by deforming it in a small-sized temporary shape in advance. Once triggered by an external stimulus such as water bath or infrared diode laser,⁴⁸ the structure could recover and show self-expanding behavior, as illustrated in Figure 1(d).

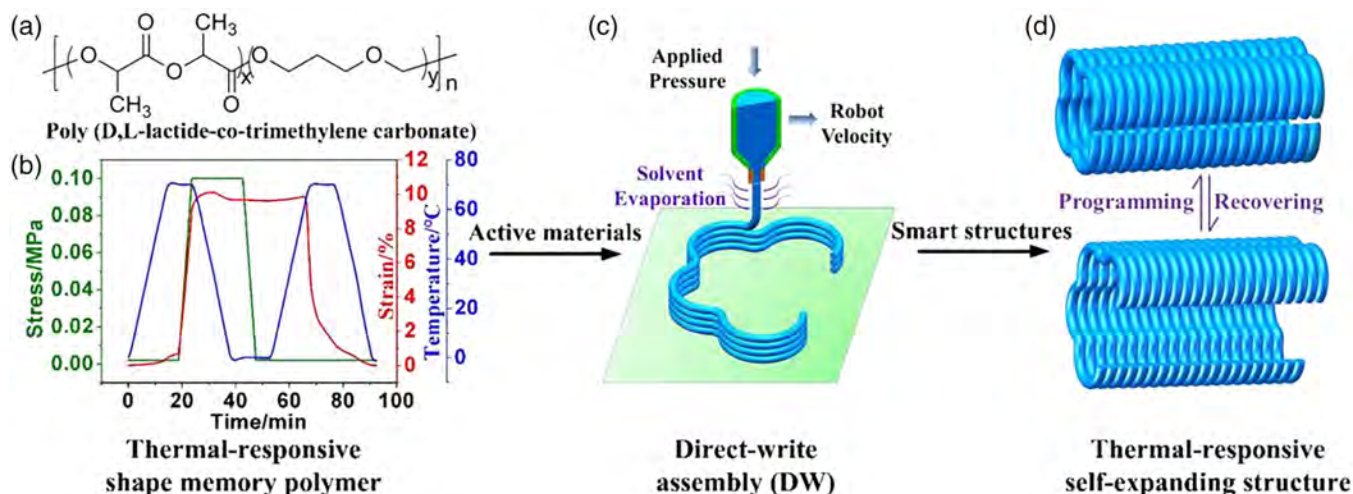


Figure 1. Fabrication procedure of 4D printing of shape memory PLMC through DIW: (a) chemical structure of PLMC; (b) shape memory performance through SMC test; (c) DIW process of PLMC ink with fast evaporation once extruded under a suitable applied pressure and robot velocity; and (d) shape memory behavior of 4D printed smart structure. [Color figure can be viewed at wileyonlinelibrary.com]

Rheological Properties

To guarantee the successful construction of customer-designed architectures, the ink requires a relatively low viscosity to flow continuously through the nozzle. However, if it is too dilute, the ink does not have excellent shape retention modulus upon deposition. Thus, the critical rheological parameter of the apparent viscosity was characterized first. Figure 2(a) is the log-log plot of process-related viscosity versus shear rate for different contents (PLMC 1/5, 1/6, and 1/7) using a 200 μm nozzle. The viscosity of the inks was remarkably affected by solution content. The process-related viscosity decreased as the shear rate increased, exhibiting a shear-thinning performance to facilitate ink flow through the nozzle. Bruneaux *et al.* reported that the process-related viscosity has dependence on printing parameters because a crystal-depleted lubrication layer usually exists near the wall of micronozzle.⁴⁵ The viscosity for PLMC 1/6 extruded from different nozzles made no evident difference as shown in Figure 2(b). It indicated that in the selected range of nozzle sizes, apparent wall slip occurred hence no obvious wall effect. This was consistent with the results of previous literature.^{41,49}

Solvent Evaporation Properties

The solvent evaporation behavior of DCM plays a critical role in the ink transition from fluid to solid which is important to retain filamentous morphology. The solvent evaporation properties of DCM were evaluated by the mass reduction of the extruded filament with time. Figure 2(c) presents the real-time solvent content of a 5 mm filament deposited using various inks through a 510 μm nozzle. The nozzle size was a minimum value for precise investigation of the mass reduction of PLMC 1/5. This was because the solvent evaporated simultaneously once the ink was forced out from the nozzle, making it hard to record the initial evaporation rate. Thus, the initial solvent fraction was lower than the nominal content in the polymer ink. The test revealed that approximately 15–30% DCM evaporated during the first 3 min for all inks. This fast evaporation rate was critical for freeform structures. PLMC 1/5 showed the shortest drying time due to the

lowest content of DCM. As to PLMC 1/6 extruded using different nozzles, the evolution of normalized DCM content (divided by the initial measured DCM content) with time was also investigated as shown in Figure 2(d). The smaller size remarkably accelerated the evaporation rate owing to the shorter diffusion distance within the filament.⁴¹ The smaller size increased the rigidity and endowed the printed structures with shape retention.

Fabrication of Various Structures

Three inks (PLMC 1/5, 1/6, and 1/7) and six nozzles (100, 160, 200, 260, 330, and 510 μm) were used to determine the appropriate conditions for different dimensional structures. The extrusion velocity changed with applied pressure for various PLMC inks [Figure 3(a)] and nozzles [Figure 3(b)]. Figure 4(a) depicts a printing map with nearly ranges of PLMC content and nozzle size to build up various structures. These plots were critical to set the corresponding velocity and applied pressure parameters for the specific ink and nozzle. A variety of 1D, 2D, and 3D microstructures were successfully fabricated based on suitable parameters. The morphologies of various printed structures are shown in Figure 4(b). Both the 1D and 2D microstructures were fabricated with PLMC 1/6 through a 200 μm nozzle. The side view and cross-sectional SEM image [Figure 4(b-i,ii)] shows that the filament was relatively smooth and its cross-sectional shape was nearly round with a diameter of 183 μm . The diameter shrinkage was about 8.5% due to the solvent evaporation. 2D patterns of the horse and the sun flower are presented in Figure 4(b-iii,iv), which were fabricated under 1.75 MPa and 1 mm s^{-1} velocity. A 3D circular tower shown in Figure 4(b-v) was built with PLMC 1/7 with 4 mm length and 400 μm radius. A 3D freeform circular spiral presented in Figure 4(b-vi) was fabricated with PLMC 1/5 through a 160 μm nozzle. Figure 4(b-vii) shows an optical graph of Gecko, which was printed using PLMC 1/6 with 45 mm length, 38 mm width, and 6 mm height. More details of printed Gecko are shown in Figure 5. It showed high similarity between the model [Figure 5(a)] and the printed object [Figure 5(b)]. Figure 5(c) depicts the cross-sectional view of Gecko in the first

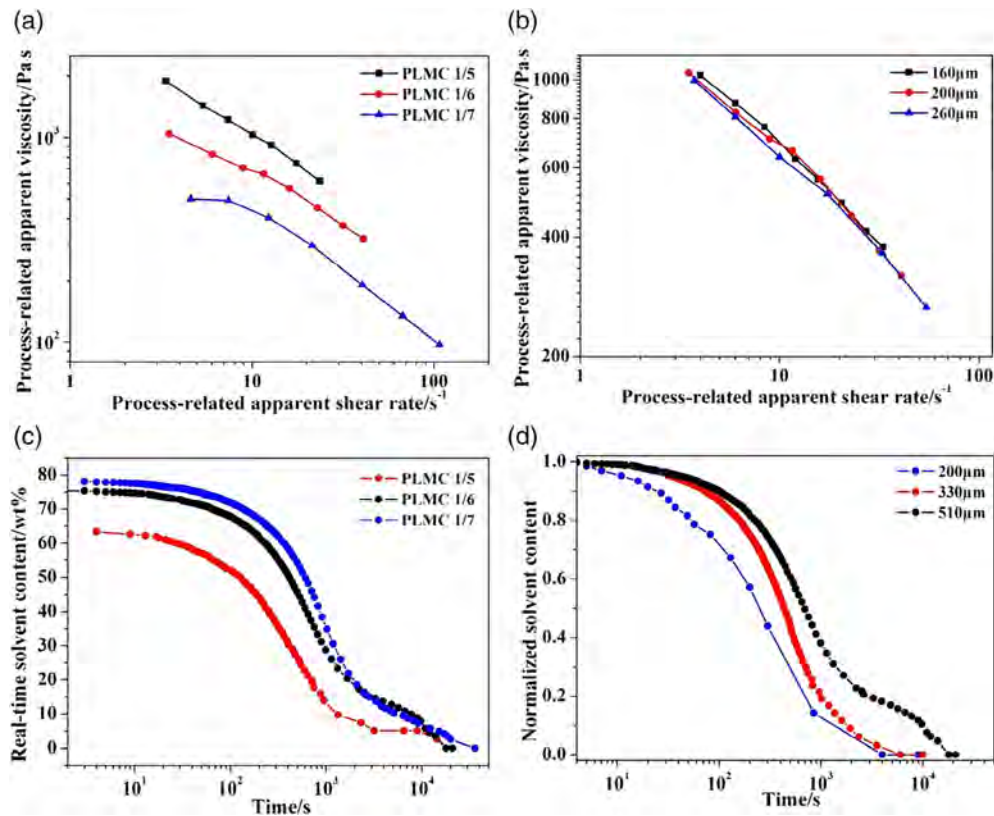


Figure 2. Properties investigation of PLMC inks for successful 3D printing: (a) apparent viscosity-shear rate plots of different inks extruded from 200 μm nozzle; (b) apparent viscosity-shear rate plots of different nozzles using PLMC 1/6; (c) real-time solvent content versus time of various inks; and (d) normalized solvent content with time of different nozzles. [Color figure can be viewed at wileyonlinelibrary.com]

few printed layers. Figure 5(d) shows the partial enlargement of suspended structure of Gecko foot. It revealed that customer-designed 3D structures of PLMC could be obtained, which extended the material's adaptability.

Mechanical Properties

Figure 6 and Table I present the static mechanical properties of the printed PLMC filaments with different printing parameters. Tensile tests revealed that the introduction of soft TMC segment led to a lower Young's modulus and a higher elongation at break

compared to PLA-based materials.^{50,51} PLMC 1/6 extruded from a nozzle of 200 μm exhibited a high tensile strength of ~ 21 MPa, Young's modulus of ~ 1059 MPa, and strain at break of $\sim 20\%$. The mechanical properties of PLMC 1/7 using a nozzle of 200 μm and PLMC 1/6 using a nozzle of 260 μm were lower. The reason was that higher solvent content or larger diameter took more time for DCM to evaporate thus more bubbles remained in the filament. A similar decrease in PLMC 1/5 using a nozzle of 200 μm and PLMC 1/6 using a nozzle of 160 μm was observed. It could be explained that the viscous ink or narrow nozzle easily

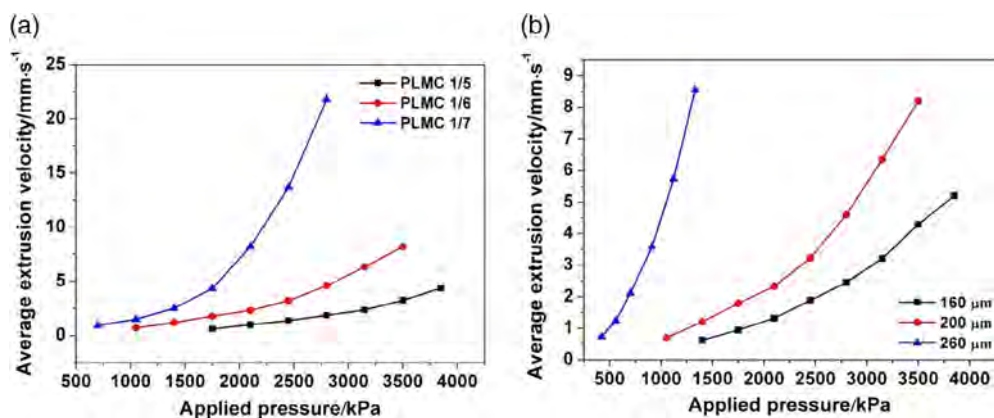


Figure 3. Average extrusion velocity rate versus applied pressure for (a) various inks (PLMC 1/5, 1/6, and 1/7) extruded from 200 μm micronozzle and (b) PLMC 1/6 printed by various nozzle diameters (160, 200, and 260 μm). [Color figure can be viewed at wileyonlinelibrary.com]

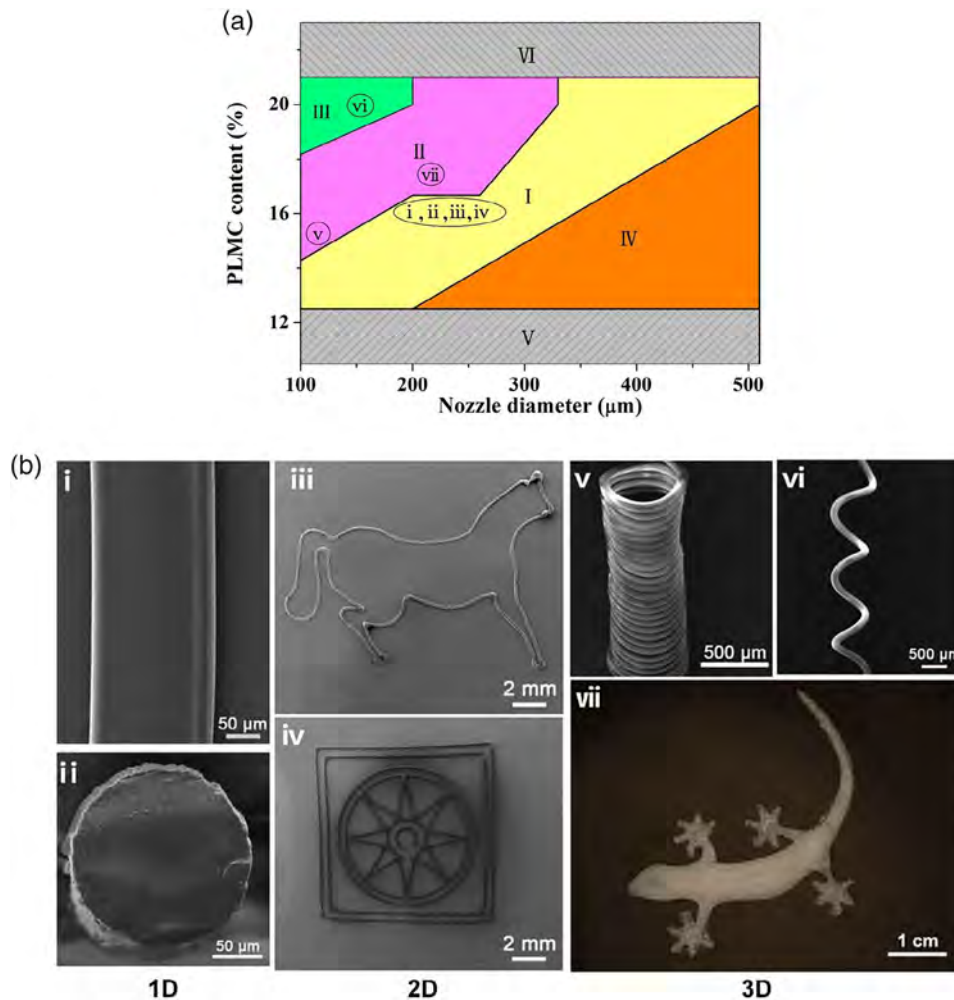


Figure 4. DIW printing of PLMC: (a) 3D printing map. Zone I: range of 1D filament and 2D architectures with one layer. Zone II: range of 3D self-supporting geometries. Zone III: range of 3D freeform structures. Zone IV: range of filaments collapse. Zone V: range where PLMC inks are too dilute to retain morphology. Zone VI: range where too viscous PLMC inks lose fluidity for consecutive extrusion. (b) Morphologies of various printed structures: (I-II) 1D filament. (III-IV) 2D patterns. (V) 3D tower. (VI) 3D freeform spiral. (VII) 3D Gecko. [Color figure can be viewed at wileyonlinelibrary.com]

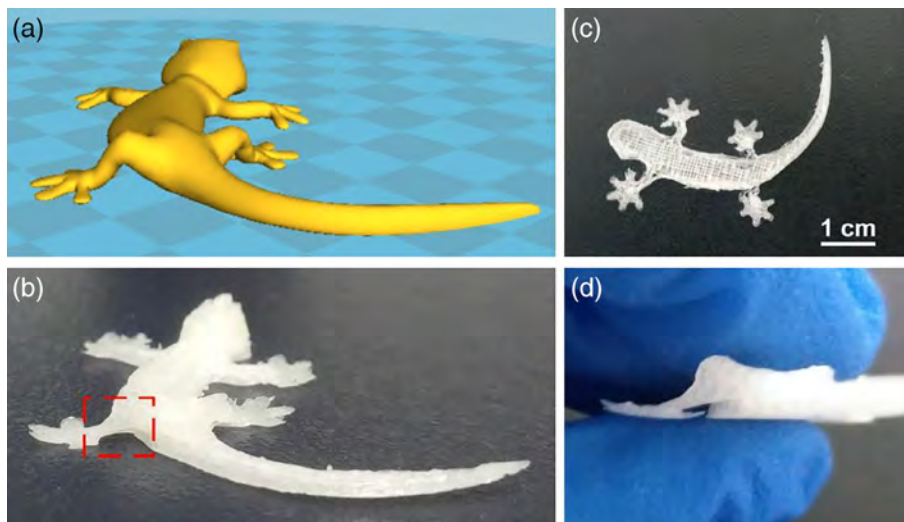


Figure 5. 3D Gecko: (a) a CATIA model; (b) printed Gecko by DIW assembly; (c) cross-sectional view of Gecko with a few layers; and (d) partial enlargement of suspended structure of Gecko foot. [Color figure can be viewed at wileyonlinelibrary.com]

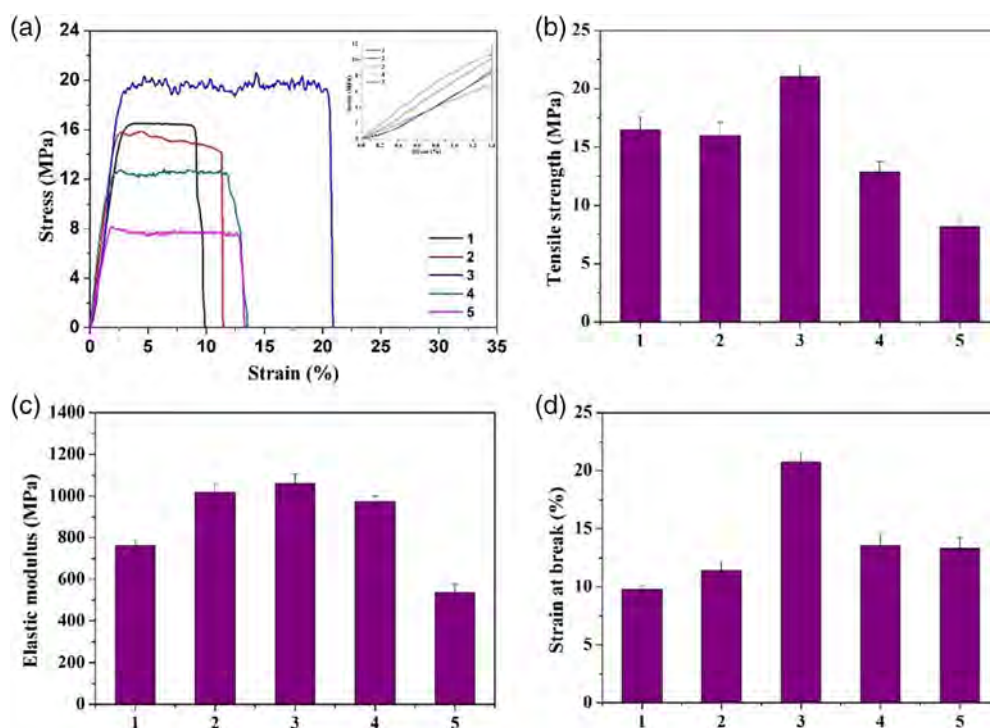


Figure 6. Mechanical properties of the PLMC filaments stretched at room temperature. (a) Tensile stress–strain plots of the printed PLMC filaments with different printing parameters; (b) tensile strength; (c) Young's modulus; and (d) strain at break (sample 1: PLMC 1/6, 260 μm ; sample 2: PLMC 1/6, 160 μm ; sample 3: PLMC 1/6, 200 μm ; sample 4: PLMC 1/7, 200 μm ; and sample 5: PLMC 1/5, 200 μm). [Color figure can be viewed at wileyonlinelibrary.com]

clogged the syringe and caused unstable extrusion (Figure S1, Supporting Information). The printing parameter with PLMC 1/6 and a 200 μm nozzle was the best choice for the best mechanical behavior.

Thermal, FTIR, and Shape Memory Performance

Based on the optimal printing parameters, the macroscopic properties of as-printed and original PLMC were evaluated. Figure 7 (a) presents storage modulus and $\tan \delta$ of these two samples versus temperature. It reflected the printing process did not change the peak of $\tan \delta$ significantly. The rubbery moduli of the original and as-printed PLMC at high temperature platform were 0.98 and 0.92 MPa, respectively. It was a negligible difference, showing good stability after printing. DSC analysis in Figure 7(b) shows that the polymer was amorphous and an endothermic peak at approximately 50 $^{\circ}\text{C}$ was observed. The glass transition temperature (T_g) determined by DSC test was lower than that by DMA.

This was due to the hysteresis of the movement of the polymer segments in DMA test. The comparison of thermal and shape memory properties between original and as-printed PLMC is illustrated in Table II. Compared to PLA,^{52,53} PLMC had a lower T_g due to the introduction of soft segment of TMC. Besides, the composition of the original and as-printed PLMC was proven and compared by ATR-FTIR spectroscopy in Figure 7(c). Both the samples showed the characteristic $\text{C}=\text{O}$ vibration peak at 1746 cm^{-1} , $\text{C}-\text{O}$ stretching peak at 1080 cm^{-1} , and $\text{C}-\text{C}$ stretching peak at 1183 cm^{-1} , which was comparable with other types of PLMC as reported in literature.^{54,55}

To quantitatively evaluate R_f and R_r , SMC test was conducted on printed samples as shown in Figure 8(a). PLMC exhibited enhanced R_f and R_r of 99.98 and 100%, respectively, showing the maintained shape memory behavior after printing process. Figure 8(b,c) visually demonstrates the macroscopic shape memory behavior of printed PLMC. The printed self-

Table I. Tensional Results of As-Printed PLMC Filaments at Room Temperature

Number	PLMC content (wt %)	Nozzle diameter (μm)	Tensile strength (MPa)	Elastic modulus (MPa)	Strain at break (%)
1	1/6	260	14.88 \pm 1.08	761.22 \pm 28.95	9.80 \pm 0.28
2	1/6	160	16.96 \pm 1.14	1018.90 \pm 43.39	11.40 \pm 0.67
3	1/6	200	21.03 \pm 0.90	1059.07 \pm 47.21	20.78 \pm 0.82
4	1/7	200	14.05 \pm 0.89	862.84 \pm 24.82	29.83 \pm 1.02
5	1/5	200	9.62 \pm 0.72	599.62 \pm 36.82	30.29 \pm 0.96

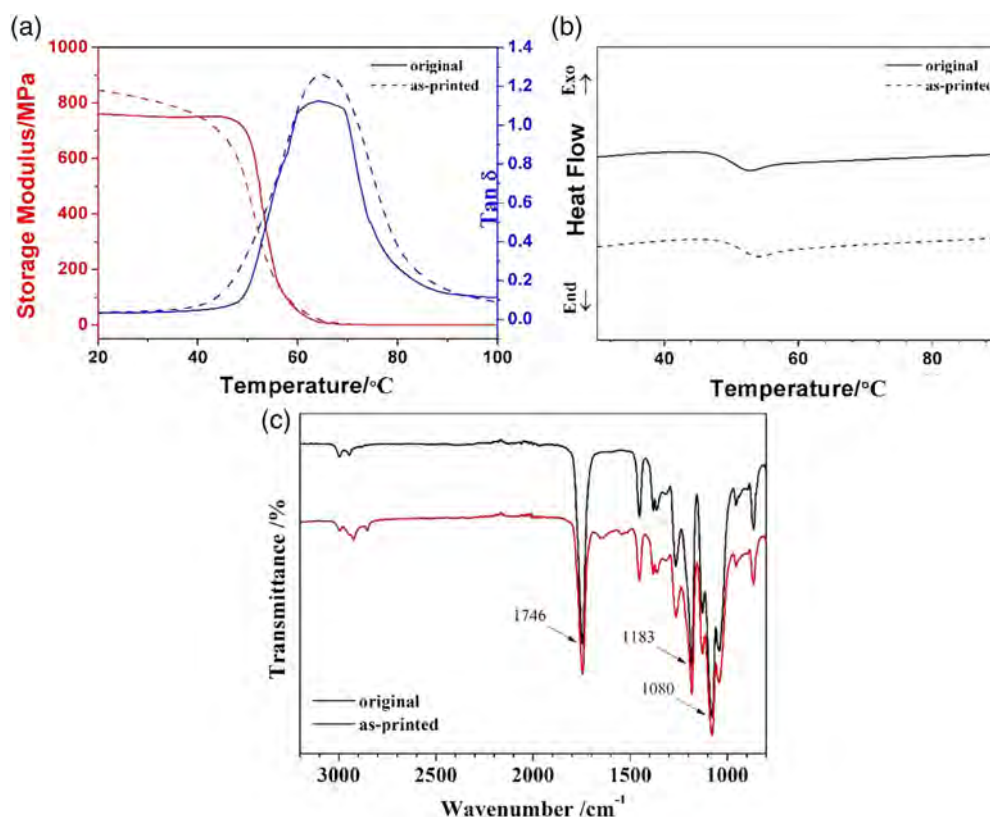


Figure 7. Comparison of original and as-printed PLMC: (a) DMA curve; (b) DSC curve; and (c) ATR-FTIR spectroscopy. [Color figure can be viewed at wileyonlinelibrary.com]

supporting 3D structures after one cycle of shape deformation could return to their initial shape with recovery ratio above 90%. We called the shape-changing process from a 3D shape to another, and then recovered to the original one as 3D–3D–3D transformation. These 3D–3D–3D shape transformations with excellent shape recovery performance paved the way for accurate 4D printing.

Characterization of Printed Scaffolds

The ORTH and DISP scaffolds (Movie S1, Supporting Information) were printed with PLMC 1/6 using a nozzle of 100 μm . Figure 9(a) shows that both scaffolds exhibited full pore interconnectivity and well-defined structures. The strut width was approximately 80 μm and the pore size was about 420 μm for ORTH and 170 μm for DISP in the horizontal plane. Furthermore, the spacing of adjacent struts in the axial direction was approximately 500 μm , which was closely in agreement with our previous design. Compared to ORTH scaffolds, the pore size of DISP almost halved, in accordance with our pre-estimation.

Table II. Comparison of Thermal and Shape Memory Properties Between Original and As-Printed PLMC

Sample	T_g by DSC ($^{\circ}\text{C}$)	T_g by DMA ($^{\circ}\text{C}$)	R_f (%)	R_r (%)
Original	49.31	64.09	99.52	99.98
As-printed	50.16	65.14	99.75	100.00

Figure 9(b) shows that the theoretical porosity volume ratios of ORTH and DISP scaffolds were 84.29 and 88.78%, respectively. The realistic porosity volume ratio was evaluated from the SEM images using eqs. (3) and (4). Herein, D , L , W , and H were the measured strut diameter, strut length, unit width, and unit height, respectively. The evaluation of realistic porosity ratio from SEM revealed the values of $89 \pm 0.92\%$ for the ORTH scaffold and $92 \pm 1.05\%$ for the DISP one. The increasing value about 2.2–5.6% was directly due to the shrinkage of the strut caused by fast solvent evaporation. These results were in agreement with reported scaffold porosities regarding bone tissue engineering.⁵³

4D Shape-Changing Behavior of Various Structures

After successfully fabricating 1D, 2D, and 3D structures, we further demonstrated the 4D shape-changing behavior of the macroscopic structures under heat stimulus. It showed that even if the reheating temperature was a little bit lower but close to T_g , the shape recovery could also occur. Herein, we demonstrated three printed structures in 1D, 2D, and 3D for potential biomedical applications.

Structure 1: 1D Self-Tightening Filament. A filament with length of 30 mm was extruded from PLMC 1/6 under 1.4 MPa and 0.5 mm s^{-1} using a nozzle of 200 μm . Then, it was stretched to 50 mm as temporary shape in a water bath at 70 $^{\circ}\text{C}$. The elongation at break of the filament was 329% at 70 $^{\circ}\text{C}$ (Figure S2, Supporting Information). Subsequently, the filament was cooled and made into a loosely knot. The self-tightening mechanism is

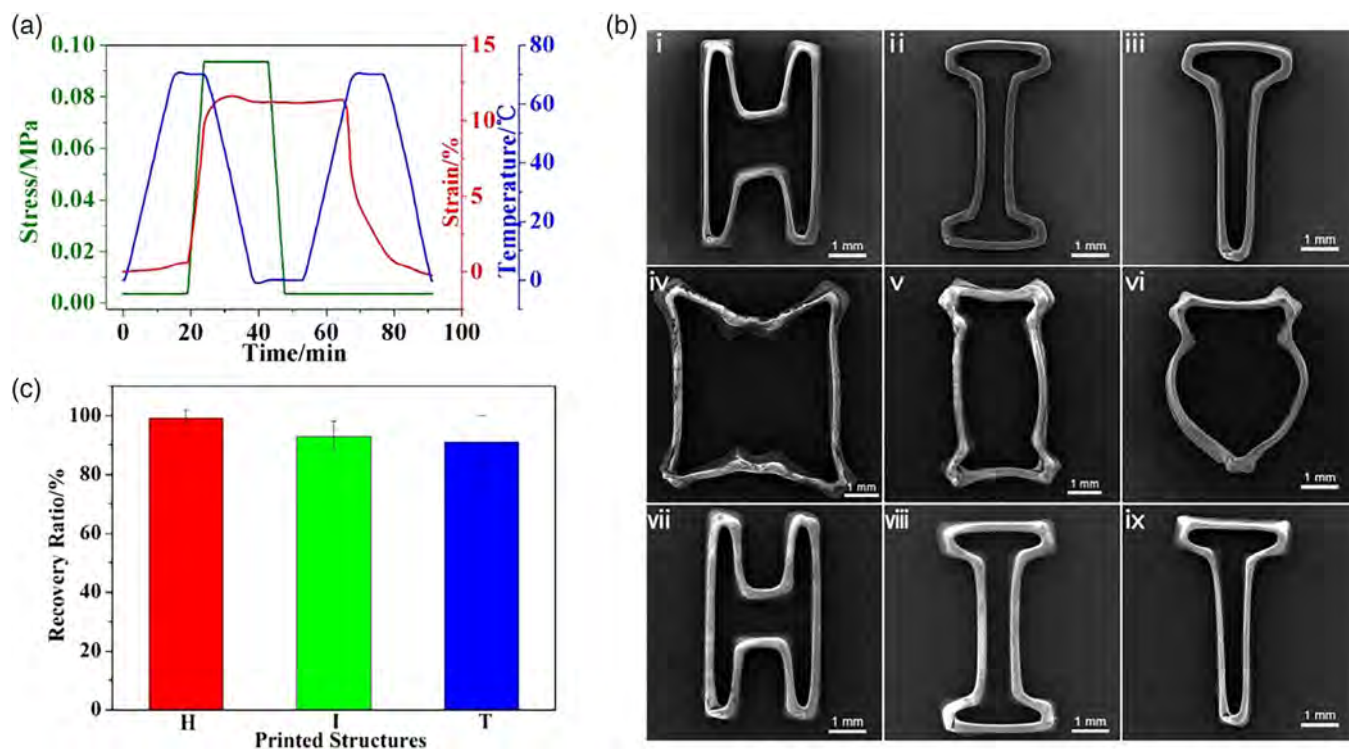


Figure 8. Shape memory properties of as-printed PLMC: (a) SMC; (b) shape-changing behavior of 3D–3D–3D structure transformations. (i–iii) Original shape. (iv–vi) Temporary shape. (vii–ix) Recovered shape; and (c) quantitative recovery ratio of the printed shape-changing structures. [Color figure can be viewed at wileyonlinelibrary.com]

illustrated in Figure 10(a–i). When the two ends of the filament were fixed and immersed in normal saline (0.9% NaCl) at 45 °C, the filament behaved shrink and closed the knot tightly, as shown in Figure 10(a–ii–v) and Movie S2 (Supporting Information). Besides, it could lower the requirement for shape recovery to save energy, reducing the risk of heating to a high temperature in biomedical field.

A further set of experiments were performed to demonstrate the self-tightening behavior of the filament in closing an incision

between two PTFE films. Here, the printed filament was painted black for a better observation. A filament with 80 mm length (original shape) was printed using PLMC 1/6 through a 200 μm nozzle. Then, it was stretched to 160 mm (temporary shape) at 70 °C. After fixing the temporary shape, the filament was used to sew two films loosely and a 1 mm gap was left between the films. At 45 °C, the filament automatically shortened and closed the gap within 4 s. The self-tightening behavior is illustrated in Figure 10(a–vi,vii).

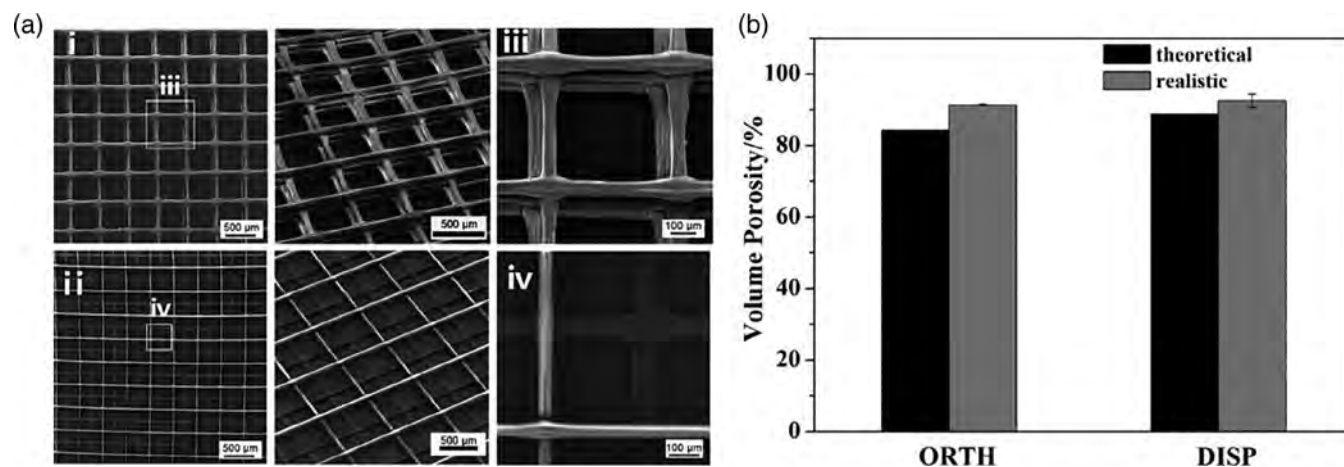


Figure 9. Scaffold characterization: (a) SEM images of printed scaffolds with (i,iii) ORTH and (ii,iv) DISP pattern and (b) theoretical and realistic volume porosity of ORTH and DISP scaffolds.

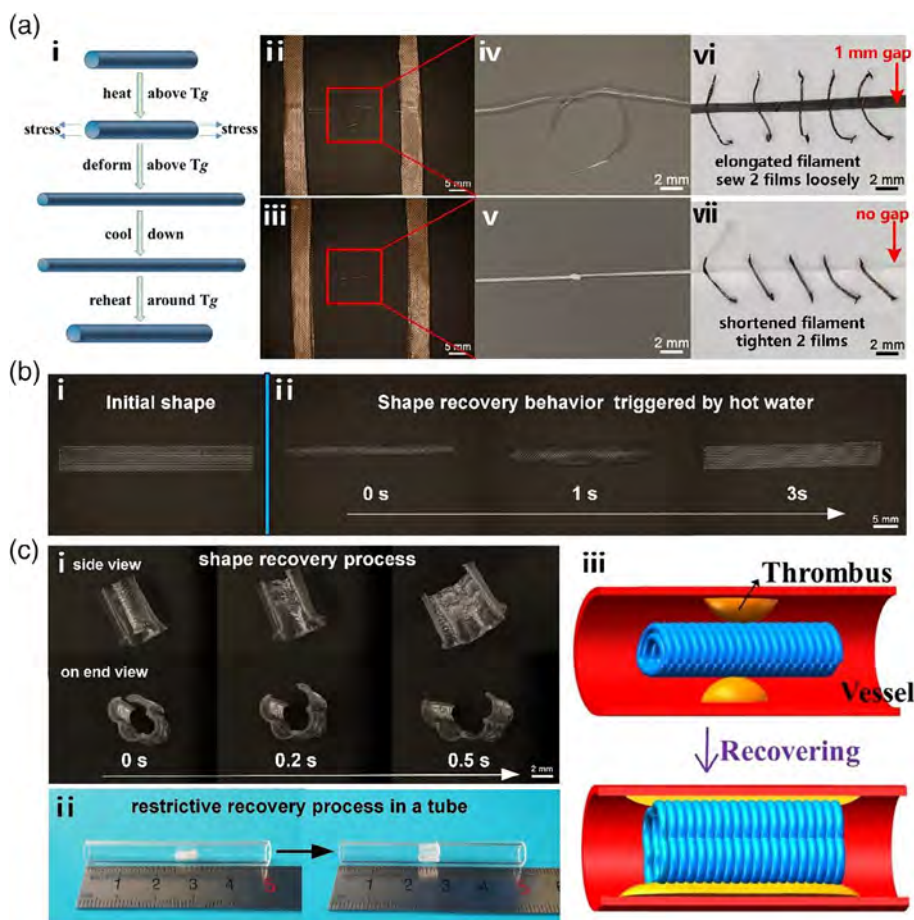


Figure 10. 4D printed shape-changing devices using PLMC 1/6 ink: (a) 1D filament. (i) Schematic of self-tightening mechanism. (ii–v) Self-tightening behavior of the filament from loosely to tightly knotted. (vi) Elongated filament sews two films loosely with a gap of 1 mm. (vii) Filament shortened under heat and closed the gap between two films; (b) 2D nonwoven fabric. (i) Initial printed shape. (ii) Photo series of the macroscopic shape recovery behavior of the fabric; and (c) 3D scaffold. (i) Macroscopic shape memory behavior of the scaffold within 0.5 s. (ii) Restrictive shape recovery process in a PMMA tube. (iii) Schematic diagram of restrictive shape recovery behavior exhibiting potential as an intravascular stent. [Color figure can be viewed at wileyonlinelibrary.com]

One of the challenges in surgery operation is how to close the incision or open lumen. Traditional methods are conducted by tying a knot in endoscopic surgery, which is difficult because it requires for high operation accuracy. Combining with intrinsic shape-changing performance of SMPs, it is expected that the surgical suture could be printed into different sizes to satisfy various demands.

Structure 2: 2D Self-Deployable Nonwoven Fabric. A multilayer nonwoven fabric with 40 mm length and 5 mm width was printed through a nozzle of 100 μm under 2.45 MPa and 0.5 mm s^{-1} . Then, wrapped the fabric into a spiral shape as the temporary shape and fixed it at room temperature. When immersed into normal saline at 45 $^{\circ}\text{C}$, the spiral recovered to its original shape within 3 s, as shown in Figure 10(b). The volumetric porosity of the smart fabric reached 90% calculated from eqs. (3) and (4). Besides, large pore size has the advantage of benefiting infiltration and permeability of blood and nutrition into the fabric, promoting its vascularization.⁵⁶ Furthermore, higher porosity ratio corresponds to higher specific surface, which could

improve the interaction between the fabric and the physiological environment. The smart textile with thermally induced shape-memory effect has potential in numerous biomedical applications such as self-adjusting implants, controlled drug release, and cell culture scaffold.

Structure 3: 3D Self-Expandable Scaffold. A multilayer flower-like self-expandable scaffold with an outer diameter of 30 mm and a height of 6 mm was printed using a micronozzle of 200 μm under 2.45 MPa and 2 mm s^{-1} . The scaffold contained 60 layers and the height of the strut was approximately 100 μm in each layer. The moving distance in z axis direction was set at 100 μm to make better adhesion between adjacent filaments. The flower-like shape was designed to increase the frictional force. The printed scaffold was deformed into a small packed shape with smaller outer diameter in advance. *In vitro*, we dipped the scaffold in normal saline at 60 $^{\circ}\text{C}$ and it showed self-expanding behavior as shown in Movie S3 (Supporting Information). Figure 10(c-i) demonstrates that the shape memory process of the scaffold could complete within 0.5 s. The shape recovery force

was measured to evaluate the shape recovery capability of the 4D scaffold [Figure S3(a), Supporting Information]. The recovery force gradually increased as the temperature increased. The recovery force peak of ~ 0.2 N reached maximum at 37.8 °C, which was a little lower than T_g . Then, it decreased rapidly in the temperature range of 37.8 – 50 °C and finally stabilized at 0.19 N. The low recovery force near to body temperature guaranteed a gentle recovery process. The load–displacement curve of the scaffold is marked in Figure S3(b), Supporting Information. It revealed that the yield strength and the fracture strength were 2 and 12.5 N, respectively, which were close to other scaffolds reported in biomedical devices.^{57,58}

In minimally invasive surgery implantation, a reduction of the external diameter of device is often desired to enter a narrow incision or lumen.⁵⁹ Further, we simulated *in vitro* shape recovery process under restrictive conditions. As shown in Figure 10(c-ii), the PMMA tube was monitored as the restrictive environment with an inner diameter of 5 mm. The printed scaffold was programmed into a temporary shape with outer diameter much smaller than the tube's inner diameter, and then implanted in the tube. When heated in normal saline at 40 °C, the scaffold showed a restrictive shape recovery process within 35 s, as shown in Movie S4 (Supporting Information). We could imagine that such a self-expandable scaffold may serve as an intravascular stent to support the thrombus in a narrow vessel. The schematic diagram in Figure 10(c-iii) exhibits great potential in minimally invasive treatment of vascular stenosis.

CONCLUSIONS

In this article, 4D shape-changing structures based on shape memory PLMC were constructed through DIW. We first achieved the 3D printing of PLMC for the first time. The viscosity of the ink was modulated to flow continuously and possess shape retention, exhibiting shear thinning behavior. The solvent evaporation rate could be accelerated by increasing the ink content or decreasing the nozzle diameter. We depicted a printing map to construct various customer-designed geometries from micro to macro, 1D to 3D. The comparison of thermal, FTIR, and shape memory properties before and after printing showed no changes. The printed shape-changing PLMC structures had low actuation temperature at 40 – 45 °C, fast responsive time at 3 – 35 s, Young's modulus >1000 MPa, tensile strength ~ 21 MPa, excellent shape recovery ratio at 99.98% , and high volume porosity at around 92% . The printed PLMC structures thus show their potential as 1D surgical suture, 2D nonwoven fabric, and 3D self-expandable stent for minimally invasive biomedical applications. Although we focus on potential biomedical applications in 4D printing, the integration of DIW with PLMC structures may open new opportunities for other development of soft robotics, microfluids, microreactor, microsensors, and beyond.

ACKNOWLEDGMENTS

This work has been financially supported by the National Nature Science Foundation of China (grant nos. 11632005 and 11672086), and Foundation for Innovative Research Groups of the National Natural Science Foundation of China under the grant no. 11421091, for which we are very grateful.

REFERENCES

1. Behl, M.; Lendlein, A. *Mater. Today*. **2007**, *10*, 20.
2. Lendlein, A.; Kelch, S. *Angew. Chem. Int. Ed.* **2002**, *41*, 2034.
3. Liu, C.; Qin, H.; Mather, P. T. *J. Mater. Chem.* **2007**, *17*, 1543.
4. Ratna, D.; Karger-Kocsis, J. *J. Mater. Sci.* **2008**, *43*, 254.
5. Yu, K.; Liu, Y.; Leng, J. *RSC Adv.* **2013**, *4*, 2961.
6. Sokolowski, W. M.; Tan, S. C. *J. Spacecraft Rockets.* **2007**, *44*, 750.
7. Zhang, R. R.; Guo, X. G.; Liu, Y. J.; Leng, J. S. *Compos. Struct.* **2014**, *112*, 226.
8. Zarek, M.; Layani, M.; Cooperstein, I.; Sachyani, E.; Cohn, D.; Magdassi, S. *Adv. Mater.* **2016**, *28*, 4449.
9. Ware, T.; Simon, D.; Hearon, K.; Liu, C.; Shah, S.; Reeder, J.; Khodaparast, N.; Kilgard, M. P.; Maitland, D. J.; Rennaker, R. L.; Voit, W. E. *Macromol. Mater. Eng.* **2012**, *297*, 1193.
10. Yang, H.; Leow, W. R.; Wang, T.; Wang, J.; Yu, J. C.; He, K.; Qi, D. P.; Wan, C. J.; Chen, X. D. *Adv. Mater.* **2017**, *29*, 1701627.
11. Ugur, G.; Chang, J. Y.; Xiang, S. H.; Lin, L. W.; Lu, J. *Adv. Mater.* **2012**, *24*, 2685.
12. Khaldi, A.; Plesse, C.; Vidal, F.; Smoukov, S. K. *Adv. Mater.* **2015**, *27*, 4418.
13. Hu, J. L.; Chen, S. J. *J. Mater. Chem.* **2010**, *20*, 3346.
14. Lendlein, A.; Langer, R. *Science*. **2002**, *296*, 1673.
15. Bodaghi, M.; Damanpack, A. R.; Liao, W. H. *Mater. Des.* **2017**, *135*, 26.
16. Wache, H. M.; Tartakowska, D. J.; Hentrich, A.; Wagner, M. H. *J. Mater. Sci. Mater. Med.* **2003**, *14*, 109.
17. Baer, G. M.; Small, W.; Wilson, T. S.; Benett, W. J.; Matthews, D. L.; Hartman, J.; Maitland, D. J. *Biomed. Eng. Online*. **2007**, *6*, 43.
18. Wischke, C.; Neffe, A. T.; Steuer, S.; Lendlein, A. *J. Control. Release*. **2009**, *138*, 243.
19. Zhang, D. W.; George, O. J.; Petersen, K. M.; Jimenez-Vergara, A. C.; Hahn, M. S.; Grunlan, M. A. *Acta Biomater.* **2014**, *10*, 4597.
20. Small, W.; Metzger, M. F.; Wilson, T. S.; Maitland, D. J. *IEEE J. Sel. Top. Quant. Electron.* **2005**, *11*, 892.
21. Boire, T. C.; Gupta, M. K.; Zachman, A. L.; Lee, S. H.; Balikov, D. A.; Kim, K.; Bellan, L. M.; Sung, H. J. *Acta Biomater.* **2015**, *24*, 53.
22. Zhang, W.; Chen, L.; Zhang, Y. *Polymer*. **2009**, *50*, 1311.
23. Balk, M.; Behl, M.; Wischke, C.; Zotzmann, J.; Lendlein, A. *Adv. Drug Deliv. Rev.* **2016**, *107*, 136.
24. Fillion, T. M.; Xu, J. W.; Prasad, M. L.; Song, J. *Biomaterials*. **2011**, *32*, 985.
25. Andronova, N.; Albertsson, A. C. *Biomacromolecules*. **2006**, *7*, 1489.
26. Pego, A. P.; Poot, A. A.; Grijpma, D. W.; Feijen, J. *J. Control. Release*. **2003**, *87*, 69.

27. Ma, Z.; Wu, Y.; Wang, J.; Liu, C. *Regener. Biomater.* **2017**, *4*, 207.
28. Bao, M.; Lou, X. X.; Zhou, Q. H.; Dong, W.; Yuan, H. H.; Zhang, Y. Z. *ACS Appl. Mat. Interfaces.* **2014**, *6*, 2611.
29. Sharifi, S.; van Kooten, T. G.; Kranenburg, H. J. C.; Meij, B. P.; Behl, M.; Lendlein, A.; Grijpma, D. W. *Biomaterials.* **2013**, *34*, 8105.
30. Yang, J.; Liu, F.; Yang, L.; Li, S. M. *Eur. Polym. J.* **2010**, *46*, 783.
31. Pego, A. P.; Siebum, B.; Van Luyn, M. J. A.; Van Seijen, X. J. G. Y.; Poot, A. A.; Grijpma, D. W.; Feijen, J. *Tissue Eng.* **2003**, *9*, 981.
32. Buttafoco, L.; Boks, N.; Engbers-Buijtenhuijs, P.; Grijpma, D. W.; Poot, A. A.; Dijkstra, P. J.; Vermes, I.; Feijen, J. J. *Biomed. Mater. Res. Part B.* **2006**, *79B*, 425.
33. Pego, A. P.; Poot, A. A.; Grijpma, D. W.; Feijen, J. J. *Mater. Sci. Mater. Med.* **2003**, *14*, 767.
34. Sharifi, S.; Grijpma, D. W. *Macromol. Biosci.* **2012**, *12*, 1423.
35. Wei, H. Q.; Zhang, Q. W.; Yao, Y. T.; Liu, L. W.; Liu, Y. J.; Leng, J. S. *ACS Appl. Mat. Interfaces.* **2017**, *9*, 876.
36. Ge, Q.; Sakhaei, A. H.; Lee, H.; Dunn, C. K.; Fang, N. X.; Dunn, M. L. *Sci. Rep.* **2016**, *6*, 31110.
37. Tibbits, S. *Architect. Des.* **2014**, *84*, 116.
38. Yu, K.; Ritchie, A.; Mao, Y.; Dunn, M. L.; Qi, H. J. *Proc. IUTAM.* **2015**, *12*, 193.
39. Yu, K.; Dunn, M. L.; Qi, H. J. *Extreme Mech. Lett.* **2015**, *4*, 9.
40. Zhang, W.; Zhang, F. H.; Lan, X.; Leng, J. S.; Wu, A. S.; Bryson, T. M.; Cotton, C.; Gu, B. H.; Sun, B. Z.; Chou, T. W. *Compos. Sci. Technol.* **2018**, *160*, 224.
41. Guo, S. Z.; Heuzey, M. C.; Therriault, D. *Langmuir.* **2014**, *30*, 1142.
42. Guo, S. Z.; Yang, X. L.; Heuzey, M. C.; Therriault, D. *Nano-scale.* **2015**, *7*, 6451.
43. Guo, S. Z.; Gosselin, F.; Guerin, N.; Lanouette, A. M.; Heuzey, M. C.; Therriault, D. *Small.* **2013**, *9*, 4118.
44. He, X.; Lei, Z.; Zhang, W.; Yu, K. *3D Print. Addit. Manuf.* **2019**, *6*, 31.
45. Bruneaux, J.; Therriault, D.; Heuzey, M. C. *J. Micromech. Microeng.* **2008**, *18*, 115020.
46. Dolog, R.; Weiss, R. A. *Macromolecules.* **2013**, *46*, 7845.
47. Xie, T. *Nature.* **2010**, *464*, 267.
48. Hearon, K.; Wierzbicki, M. A.; Nash, L. D.; Landsman, T. L.; Laramy, C.; Lonnecker, A. T.; Gibbons, M. C.; Ur, S.; Cardinal, K. O.; Wilson, T. S.; Wooley, K. L.; Maitland, D. J. *Adv. Healthc. Mater.* **2015**, *4*, 1386.
49. Barnes, H. A. *J. Non-Newtonian Fluid Mech.* **1995**, *56*, 221.
50. Li, N. Y.; Li, Y. G.; Liu, S. T. *J. Mater. Process. Technol.* **2016**, *238*, 218.
51. Lanzotti, A.; Grasso, M.; Staiano, G.; Martorelli, M. *Rapid Prototyp. J.* **2015**, *21*, 604.
52. Leist, S. K.; Gao, D.; Chiou, R.; Zhou, J. *Virtual Phys. Prototyp.* **2017**, *12*, 290.
53. Serra, T.; Planell, J. A.; Navarro, M. *Acta Biomater.* **2013**, *9*, 5521.
54. Bao, M.; Wang, X. L.; Yuan, H. H.; Lou, X. X.; Zhao, Q. H.; Zhang, Y. Z. *J. Mater. Chem. B.* **2016**, *4*, 5308.
55. Chapanian, R.; Amsden, B. G. *Eur. J. Pharm. Biopharm.* **2010**, *74*, 172.
56. Gupte, M. J.; Swanson, W. B.; Hu, J.; Jin, X. B.; Ma, H. Y.; Zhang, Z. P.; Liu, Z. N.; Feng, K.; Feng, G. J.; Xiao, G. Y.; Hatch, N.; Mishina, Y.; Ma, P. X. *Acta Biomater.* **2018**, *82*, 1.
57. Jia, Y. T.; Wang, W. Z.; Zhou, X. J.; Nie, W.; Chen, L.; He, C. L. *Polym. Chem.* **2016**, *7*, 2553.
58. Rizvi, M. S.; Kumar, P.; Katti, D. S.; Pal, A. *Acta Biomater.* **2012**, *8*, 4111.
59. Zarek, M.; Mansour, N.; Shapira, S.; Cohn, D. *Macromol. Rapid Commun.* **2017**, *38*, 1600628.